Available online at www.sciencedirect.com
ScienceDirect
Nuclear Physics A 813 (2008) 199–211
NUCLEAR PHYSICS A
www.elsevier.com/locate/nuclphysa

Neutron decay spectroscopy of neutron-rich oxygen isotopes

N. Frank [a,b,c,*,1], T. Baumann [b], D. Bazin [b], B.A. Brown [a,b], J. Brown [d], P.A. DeYoung [e], J.E. Finck [f], A. Gade [a,b], J. Hinnefeld [g], R. Howes [h], J.-L. Lecouey [b,2], B. Luther [c], W.A. Peters [a,b,3], H. Scheit [b,4], A. Schiller [b], M. Thoennessen [a,b], J. Tostevin [i]

[a] *Department of Physics and Astronomy, Michigan State University, East Lansing, MI 48824, USA*
[b] *National Superconducting Cyclotron Laboratory, Michigan State University, East Lansing, MI 48824, USA*
[c] *Department of Physics, Concordia College, Moorhead, MN 56562, USA*
[d] *Department of Physics, Wabash College, Crawfordsville, IN 47933, USA*
[e] *Department of Physics, Hope College, Holland, MI 49423, USA*
[f] *Department of Physics, Central Michigan University, Mt. Pleasant, MI 48859, USA*
[g] *Department of Physics and Astronomy, Indiana University at South Bend, South Bend, IN 46634, USA*
[h] *Department of Physics, Marquette University, Milwaukee, WI 53201, USA*
[i] *Department of Physics, Faculty of Engineering and Physical Sciences, University of Surrey, Guildford, Surrey GU2 7XH, United Kingdom*

Received 13 August 2008; received in revised form 4 September 2008; accepted 9 September 2008

Available online 18 September 2008

Abstract

Neutron decay spectroscopy of neutron-rich oxygen isotopes has been performed using the two-proton knock-out reaction ^{9}Be(^{26}Ne, X)^{24,23,22}O. A combination of the knock-out of valence and core protons can explain the three observed spectra. These knock-out processes are selective and preferentially populate hole states. The observed narrow resonance state in ^{23}O at an excitation energy of 2.8(1) MeV was assigned to the $5/2^{+}$ state.

* Corresponding author.
E-mail address: nfrank@iwu.edu (N. Frank).

[1] Present address: Physics Department, Illinois Wesleyan University, Bloomington, IL 61701, USA.

[2] Present address: Laboratoire de Physique Corpusculaire, IN2P3, 14050 Caen, France.

[3] Present address: Department of Physics and Astronomy, Rutgers, The State University of New Jersey, Piscataway, NJ 08854, USA.

[4] Present address: Nishina Center for Accelerator Based Science, RIKEN, Wako, Saitama 351-0198, Japan.

0375-9474/$ – see front matter
doi:10.1016/j.nuclphysa.2008.09.009

PACS: 21.10.Pc; 23.90.+w; 25.60.Gc; 29.30.Hs

Keywords: NUCLEAR REACTIONS ^{9}Be(^{26}Ne, X)^{22,23,24}O, $E = 86$ MeV/nucleon; measured fragment and neutron energy- and angular-spectra, (fragment)(neutron)-coin, neutron decay energy spectra; deduced reaction mechanism features. ^{23}O observed unbound state

1. Introduction

It has been established that in nuclei far from stability the traditional shell ordering can change, where some energy gaps between orbitals decrease or even disappear [1,2] and others appear or widen [3]. Current shell model calculations suggest large gaps at $N = 14$ and 16 for ^{22}O and ^{24}O, respectively [4]. These shell gaps result from the shifted energies of the $0d_{5/2}$, $1s_{1/2}$ and $0d_{3/2}$ orbitals of neutrons in oxygen isotopes near the drip line. The spin–isospin component of the nucleon–nucleon force has been suggested as the reason for this change in structure [5,6] resulting in an additional attraction between protons and neutrons of the same orbital angular momentum (l) and opposite spin, i.e., $j_> = l + 1/2$ and $j_< = l - 1/2$. Thus the overlap of wave functions for a neutron in the $0d_{3/2}$ orbital and a proton in the $0d_{5/2}$ orbital results in increased binding [7]. This could explain why the addition of one proton in the $0d_{5/2}$ orbital results in ^{26}F being bound while ^{25}O is unbound.

The first experimental evidence for a widening of the $N = 16$ shell gap near the neutron drip line was found in one-neutron separation-energy systematics [8]. To quantify this energy gap for $N = 16$ between the $0d_{3/2}$ and $1s_{1/2}$ orbitals, a search for bound excited states in ^{23,24}O was performed [9]. The lack of bound excited states provided further evidence for a large shell gap in ^{23,24}O and the $3/2^+$ particle state of ^{23}O was observed in the ^{2}H(^{22}O,^{23}O)^{1}H reaction at an excitation energy of 4 MeV [10]. The recent measurement of the neutron unbound ground state of ^{25}O deduced an energy gap for the $1s_{1/2}$ and the $0d_{3/2}$ orbitals to be 4.86(13) MeV, establishing the $N = 16$ gap [11]. The first evidence of the $N = 14$ gap was deduced from the high excitation energy of the first 2^+ state in ^{22}O [12].

In the present work, a search for unbound excited states in the neutron-rich oxygen isotopes ^{22,23,24}O was performed using a two-proton knock-out reaction from ^{26}Ne. The first observation of a narrow resonance in ^{23}O has already been reported [13]. Two-proton knockout reactions with beams of intermediate-energy heavy-ions have been successfully used to explore the structure of neutron-rich nuclei [14,15]. The experimental evidence that these reactions are direct means they yield structure information about the populated states.

2. Experimental setup

The experiment was performed at the National Superconducting Cyclotron Laboratory (NSCL) at Michigan State University. The primary beam of 140 MeV/u ^{40}Ar impinged on a 893 mg/cm^2 Be production target. The average beam intensity was 105 pnA. The fragments of interest were separated by the A1900 fragment separator [16]. An achromatic 750 mg/cm^2 thick acrylic wedge degrader was placed at the dispersive intermediate image of the A1900 to achieve isotopic separation of the secondary ^{26}Ne beam. Some neutron–fragment coincidence data were recorded with the momentum slits at the intermediate image set an acceptance of 1% and some with an acceptance of 3%. The ^{26}Ne beam energy at the end of the A1900 was 86 MeV/u.

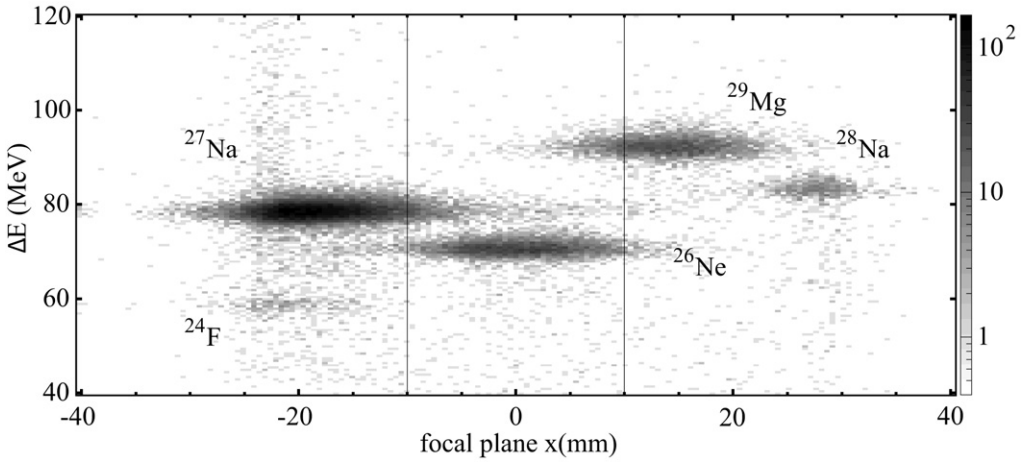

Fig. 1. ^{26}Ne beam selection plot from the A1900 fragment separator. The vertical lines in the plot indicate the location of the horizontal slits at the final focal plane of the fragment separator.

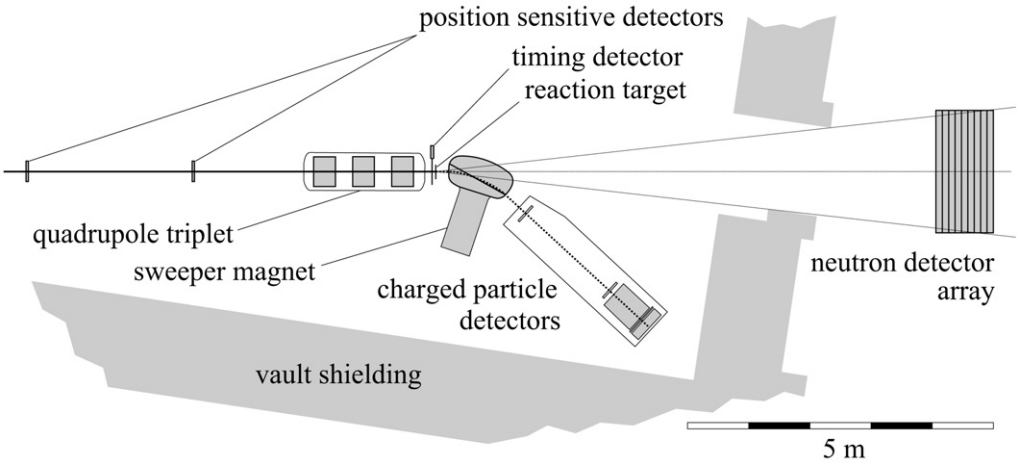

Fig. 2. The MoNA/Sweeper experimental setup [17,18].

Fig. 1 shows the composition and corresponding positions of secondary beam particles at the A1900 focal plane. The main contaminants, ^{27}Na and ^{29}Mg, were reduced by ± 10 mm slits at the focal plane as indicated by the vertical lines in Fig. 1. A ^{26}Ne beam purity of about 93% was achieved with a particle rate of about 7000/s. A plastic scintillator at the end of the A1900 provided an event-by-event start time of the secondary beam particles.

The secondary beam entered the experimental setup shown in Fig. 2. Trajectories of incoming secondary beam particles were measured using two 15×15 cm^2 position-sensitive parallel plate avalanche counters (PPACs) with a pad pitch of 1.27 mm. A quadrupole triplet downstream from the PPACs focused the beam onto the reaction target. The resolution of the position measurement at the target was 2.4 mm (note, all resolutions are quoted in terms of Full Width at Half Maximum (FWHM)). A 0.254 mm thick scintillator was placed directly in front of the 721 mg/cm^2 thick Be

reaction target to determine the time-of-flight of the secondary beam. The distance between this target scintillator and the A1900 timing scintillator was 35.7 m. The neutron-unbound isotopes of interest produced in the reaction target immediately decayed into a charged fragment and a neutron. Due to the high velocity of the incoming secondary beam the charged fragments and the neutrons were strongly forward focused. A large-gap sweeper magnet bent the charged fragments away from the neutrons which were detected at zero degrees.

The superconducting 4 Tm sweeper magnet has a vertical gap of 14 cm and a bending angle of 43° [19]. It was designed and constructed at the National High Magnetic Field Laboratory at Florida State University. For the neutron–fragment coincidence data the magnetic field was set to 3.5232 Tm. A suite of detectors behind the sweeper magnet measured particle trajectories and provided particle identification. Two 30×30 cm^2 position sensitive cathode-readout drift chambers (CRDCs), separated by 1.87 m, allowed the fragment position and direction to be measured. The resolution of the extracted angles was 2.4 mrad. Energy losses in a 65 cm long ion chamber (ΔE_{IC}) and a 40×40 cm^2, 4.5 mm thin (ΔE_{Sc}) plastic scintillator provided the separation and identification of elements. The IC pulse-height signal was corrected for the drift time within the detector volume. The particles stopped in a 15 cm thick plastic scintillator where the remaining kinetic energy (RKE) was measured. The pulse-heights of the thin and the thick scintillators were corrected for position dependence in both the dispersive and non-dispersive directions.

Neutrons were detected in the Modular Neutron Array (MoNA) [20,21] placed at a distance of 8.2 m from the reaction target. MoNA consists of 9×16 stacked 2 m long plastic scintillator bars with photomultiplier tubes (PMT) on both ends. Horizontal position and neutron time-of-flight (ToF) are determined from the time difference and the mean time, respectively, of the two PMT signals with resolutions of ~ 12 cm and ~ 0.24 ns. The detectors are shadowed vertically by the gap of the sweeper magnet and horizontally by an opening in the shielding wall in front of MoNA shown in Fig. 2. The horizontal opening shields many neutrons near the edges of the detector bars. The allowed straight-line paths from the target through the openings translate into an opening angle of $\pm 3.17°$ in the vertical direction and $-6.45°$ to $4.64°$ in the horizontal direction.

3. Data analysis

The decay energy spectra for ^{22,23,24}O* were calculated by the invariant mass method using the relativistic four-momentum vectors of the neutron and ^{21,22,23}O in the lab frame. This required the determination of the angles and energies of the neutrons and the fragments. However, first it was necessary to cleanly identify the ^{26}Ne secondary beam and the produced fragments. The ^{26}Ne beam particles were separated event-by-event by the difference in ToF between the A1900 timing scintillator and the target scintillator as shown in Fig. 3.

The fragments recorded in the charged particle detectors behind the sweeper magnet were separated first by element and then by isotope. The left side of Fig. 4 shows the energy loss as measured by the IC versus the energy loss in the thin scintillator. Nitrogen, oxygen, fluorine as well as scattered neon can be clearly identified and the oxygen isotopes were selected with the two-dimensional gate shown in left panel of Fig. 4. The oxygen isotopes were then separated by gating on the RKE versus an adjusted ToF spectrum as shown in the middle panel of Fig. 4. This adjusted ToF was calculated from the timing between the thin scintillator and the target scintillator. It was corrected for energy spread and path length differences through the magnet and in the thin scintillator.

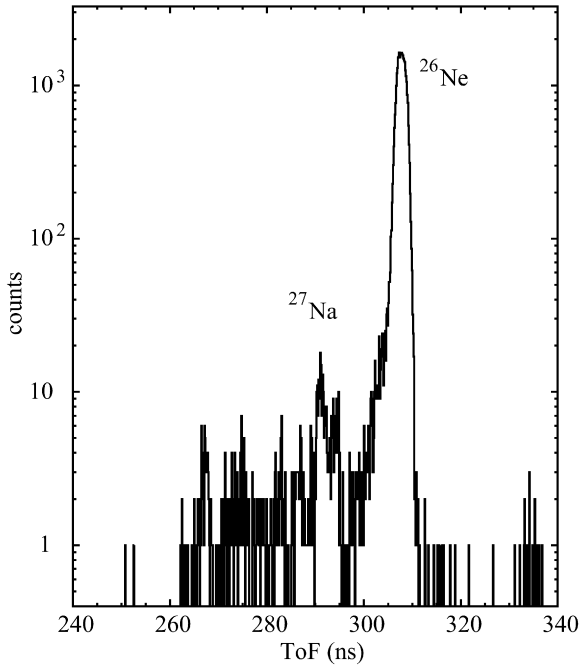

Fig. 3. Time-of-flight (ToF) between the A1900 timing scintillator and the scintillator in front of the reaction target.

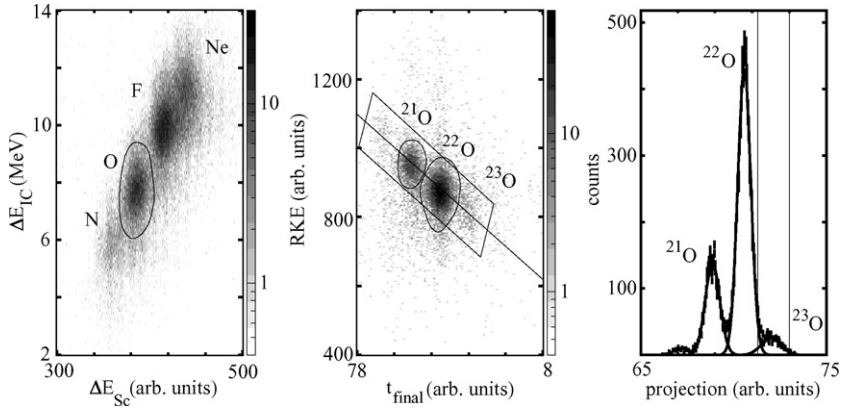

Fig. 4. Energy loss in the ionization chamber ΔE_{IC} versus energy loss in the thin scintillator ΔE_{Sc} (left), RKE scintillator energy versus adjusted ToF (middle), and the projection taken along the solid line on the RKE versus adjusted ToF plot where the solid curves represent Gaussian fits of the ^{21,22,23}O isotopes (right). The parallelogram on the RKE versus adjusted ToF plot shows the accepted events along the projection line.

The right panel of Fig. 4 shows the final isotope separation produced by taking a straight line projection through the isotopes. The solid lines are for fits with three Gaussian distributions for ^{21,22,23}O. The experimental setup required a fragment–neutron coincidence that prevented observation of ^{24}O.

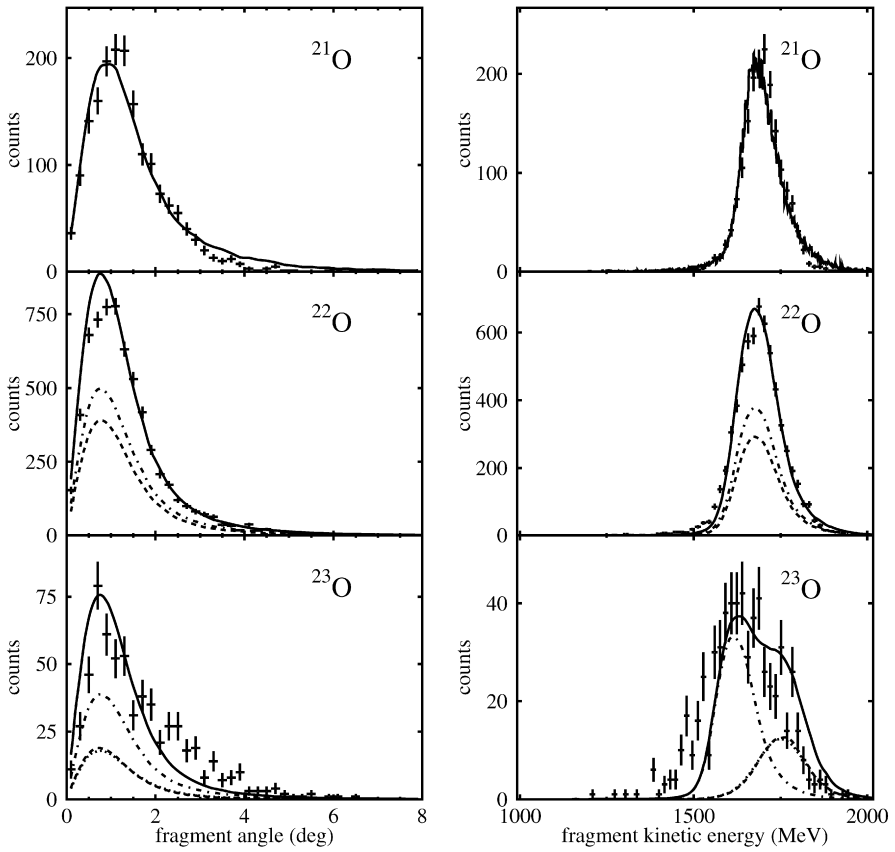

Fig. 5. Angles (left) and energies (right) at the reaction target for ^{21}O (top), ^{22}O (middle) and ^{23}O (bottom) isotopes in coincidence with neutrons. The smooth lines are results of simulations described in Section 4.

The energy and the angle of the fragments at the target position were reconstructed from the trajectories following the magnet. This was achieved with a method that takes into account the measured position at the target in the dispersive direction [22]. The ion-optical transformation matrix was produced using COSY INFINITY [23] based on measured magnetic field maps. The angle and energy resolution of the fragments as emitted from the target was 6.4 mrad and 0.9 MeV/u, respectively. Fig. 5 shows the fragment angular distribution (left) and the fragment kinetic energies (right) for ^{21,22,23}O fragments. The kinetic energy is a sum of the reconstructed energy and the average energy loss of the fragment through half of the reaction target. The peak of the angular distributions increases with decreasing mass of the fragment which is consistent with a direct production mechanism or with an increasing number of emitted particles. The kinetic energies decrease with increasing mass because of the acceptance of the sweeper magnet which cuts off fragments with lower momentum, especially for ^{21}O. The large width of kinetic energies of the ^{23}O fragments could be due to contaminations from the much more strongly populated ^{22}O which could not be completely separated as shown in Fig. 4. The smooth lines in this and the following two figures are the results of simulations which are described in more detail in Section 4.

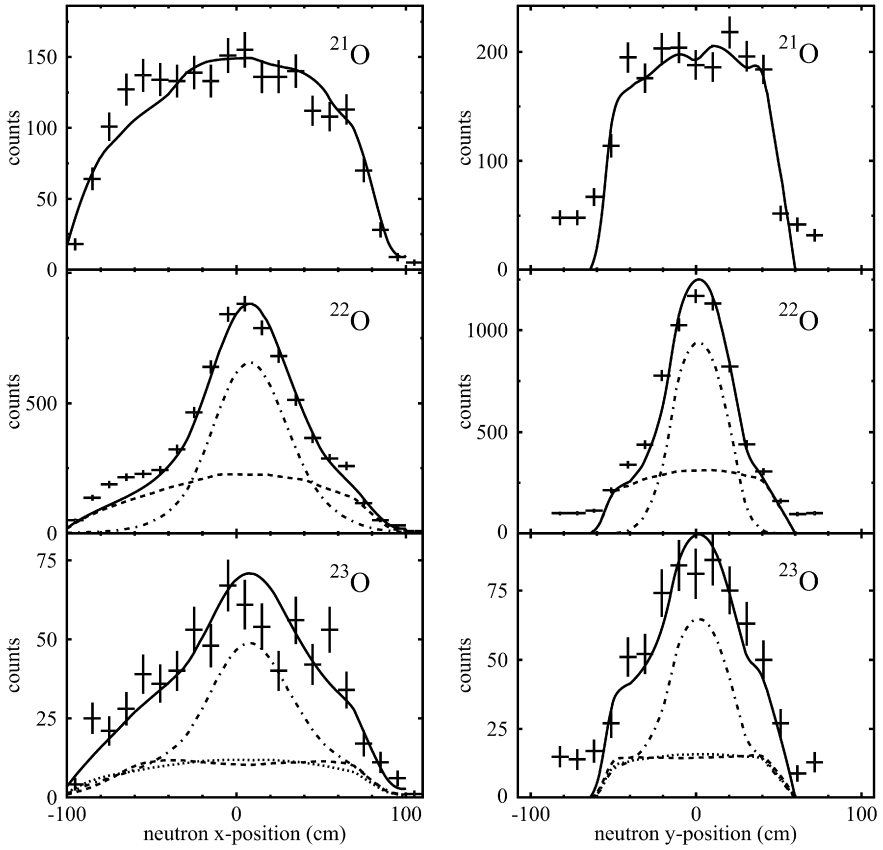

Fig. 6. Horizontal (left) and vertical (right) positions of neutrons in coincidence with ^{21}O (top), ^{22}O (middle) and ^{23}O (bottom) isotopes. The smooth curves are results of simulations described in Section 4.

Neutrons were detected with MoNA in coincidence with the ^{21,22,23}O fragments. The kinetic energy of the neutrons was calculated from the ToF between the target scintillator and the time measured by MoNA. A cut was applied to eliminate γ rays from reactions in the target [24].

The positions in the horizontal and vertical directions of the earliest neutron signal in coincidence with each of the three oxygen isotopes are shown in Fig. 6. While in the horizontal direction neutrons within the acceptance are observed along the full width of MoNA (2 m), the limited vertical acceptance results in only about 1 m being illuminated vertically. This is consistent with the shadowing of MoNA due to the vertical gap of the sweeper magnet. The sharp peak visible for neutrons in coincidence with ^{22}O is already a first indication for the emission of low-energy neutrons in the center-of-mass frame of ^{23}O. In contrast, neutrons in coincidence with ^{21}O show a completely flat distribution, while there is some evidence for a broader peak for ^{23}O coincidence data. Again, this peak could be due to contaminations from ^{22}O which could not be completely separated as shown in Fig. 4.

The azimuthal angles of the neutrons were derived from the interaction point in MoNA relative to the beam axis. The angle and energy resolutions as calculated from the measured parameters were 19 mrad and 3.8 MeV, FWHM, respectively. Fig. 7 shows the angles and the kinetic energy distributions for neutrons in coincidences with ^{21,22,23}O fragments. The sharp peaks in the angle

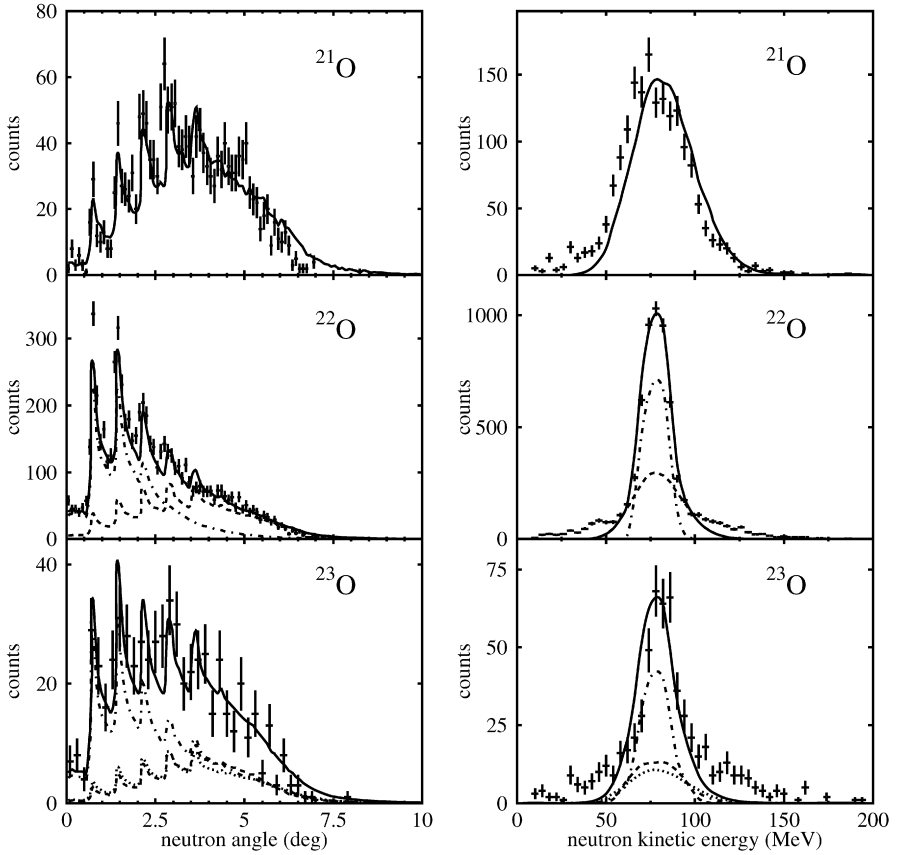

Fig. 7. Neutron angles (left) and energies (right) at the reaction target in coincidence with ^{21}O (top), ^{22}O (middle) and ^{23}O (bottom) isotopes. The smooth lines are the results of simulations described in Section 4.

spectra, especially at small angles, are due to the fact that the vertical position is known only in increments of 10 cm from the vertical position of the bar. The neutron angular distributions and the energy spectra support the observations from the position spectra. Neutrons in coincidence with ^{22}O show a narrow energy peak and small angles indicating small decay energies in ^{23}O. The contributions at small angles in the neutron spectra in coincidence with ^{23}O may result from the ^{22}O contamination in the data. As in the previous two figures the smooth curves are results from simulation which will be described in Section 4.

Monte Carlo simulations that include the geometric acceptances, intrinsic efficiencies and resolutions of all detectors were performed in order to extract the properties of the excited states from the data. The reaction mechanism was described by a Glauber reaction model [25]. Angular straggling and energy loss in the target were also included.

The unbound resonances were included in the simulations in the form of a Breit–Wigner distribution parameterized by a resonance energy (E_r) and width (Γ) [26]. In addition, a non-resonant background distribution was simulated by a Maxwellian or thermal distribution $F(E) \sim \sqrt{E}e^{-E/T}$ where the temperature T (in MeV) was a free parameter [27].

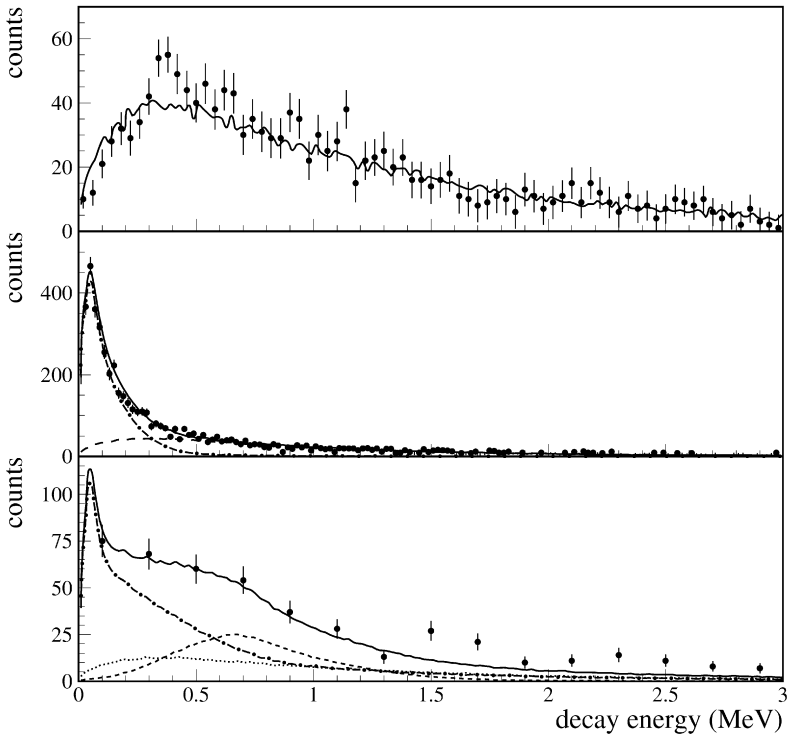

Fig. 8. Decay energy spectra of ^{22,23,24}O* (data points). The smooth curves are results from simulations; see text for details.

4. Results and discussion

The decay energy spectra for the decay of ^{22,23,24}O to ^{21,22,23}O, respectively, are shown in Fig. 8. While the ^{22}O and ^{24}O data show a broad distribution, the spectrum for ^{23}O peaks sharply at very low decay energies.

The ^{22}O (top) can be described with a non-resonant background simulated by a thermal distribution with a temperature of 1.6 MeV. The ^{23}O spectrum (middle) was fit with the sum (solid) of a low-lying resonance of 45(2) keV (dash-dotted) and a thermal distribution of temperature 0.95 MeV (dashed). The apparent observed (100 keV) width of the narrow peak is due to the experimental resolution and only an upper limit of 30 keV for the width can be extracted from the data. The statistics for the ^{24}O spectrum (bottom) are low and, as indicated already by the neutron position and angle spectra, these data could be contaminated by a non-resolved contribution from the much more strongly populated ^{23}O. The data could be reasonably described with a resonance at 700 keV and a width of 100 keV (dash), a non-resonant background with a temperature of 1.5 MeV (dotted) in ^{24}O in addition to the ^{23}O contamination (dash-dotted). Although such a resonance is consistent with the data, the spectrum could also be described with a sum (solid) of the ^{23}O background (dot-dashed) and a non-resonant background (dotted) simulated by a temperature of 2 MeV, shown in Fig. 9. The result of these simulations, which describe the three decay-energy spectra well, also reproduce the individual fragment angles and energies (Fig. 5),

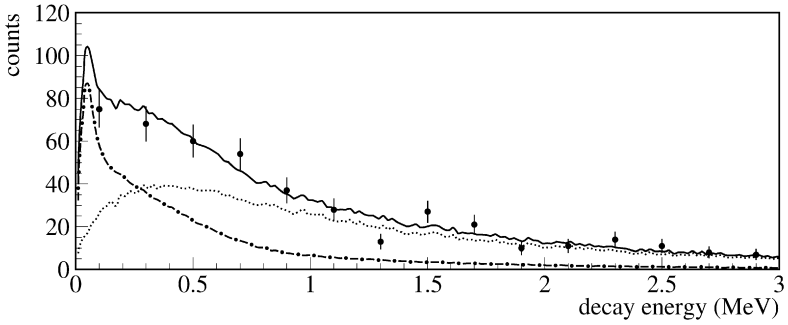

Fig. 9. Decay energy spectrum of ^{24}O. The thin smooth line corresponds to a sum of simulations of ^{23}O contaminations (dot-dashed) and a non-resonant background in ^{24}O with a temperature of 2 MeV (dotted).

neutron x- and y-positions (Fig. 6), and, neutron angles and energies (Fig. 7). The individual contributions shown in these figures for ^{23}O and ^{24}O are the same as in Fig. 8.

The observed decay energy spectra for all three isotopes can be explained within a direct reaction description of the two-proton knockout from ^{26}Ne. The dominant shell-model configuration of the ^{26}Ne ground state is two sd-shell protons coupled to a ^{24}O core [28]. Thus, the two-proton knockout [29] from ^{26}Ne can proceed by removal of two protons from the sd-shell, one proton from the sd-shell and one from the p-shell, or two protons from the p-shell. These would result in ^{24}O configurations of $\pi(0p_{1/2,3/2})^6$, $\pi(0p_{1/2,3/2})^{-1}\pi(0d_{5/2})^1$, and $\pi(0p_{1/2,3/2})^{-2}\pi(0d_{5/2})^2$, respectively.

The most obvious direct reaction is the removal of the two protons in the sd-shell. This leads predominantly to the ground-state of ^{24}O which is particle stable and does not decay by the emission of a neutron. With the full sd-shell model wave function [30,31], the cross section to the 2^+ state of ^{24}O is over a factor of ten smaller than that for populating the ground state. Such a small contribution is consistent with the low statistics observed for ^{24}O and the tentative observation of a resonance state at about 700 keV shown in the bottom panel of Fig. 8. This would correspond to an excitation energy of about 4.8 MeV in ^{24}O assuming the neutron decays to the ground state of ^{23}O. This assumption is justified because ^{23}O does not have any bound excited states [9]. However, this assignment is only tentative because the spectrum could also be described without a contribution from a resonance in ^{24}O as shown in Fig. 9.

The knockout of one proton from the sd-shell and one from the p-shell, resulting in a ^{24}O configuration of $\pi(0p_{1/2,3/2})^{-1}\pi(0d_{5/2})^1$, is a more complicated situation. This proton configuration has negative parity and so will mix with neutron excitations of the form $\nu(0p)^{-1} \times \nu(0d_{3/2})^1$ (case a), $\nu(0d_{5/2})^{-1} \times \nu(0f1p)^1$ (case b), and $\nu(1s_{1/2})^{-1} \times \nu(0f1p)^1$ (case c). Fig. 10 shows the possible admixtures of the proton excitation (π) with the neutron excitations (ν). The first two cases (a, b) would emit a high-energy neutron leading to the $5/2^+$ and $1/2^+$ states in ^{23}O, respectively [32]. The efficiency of the current setup for detection of these high-energy neutrons is very small. The $1/2^+$ state corresponds to the ground state of ^{23}O which does not emit neutrons. This leaves the first excited $5/2^+$ state which we assign to the observed low-energy peak shown in the middle panel of Fig. 8. The last case (c) has a large spectroscopic overlap with high-lying negative-parity excitations in ^{23}O and most probably decays by the emission of two or more neutrons, thus contributing to the non-resonant background in coincidence with ^{21}O shown in the top panel of Fig. 8.

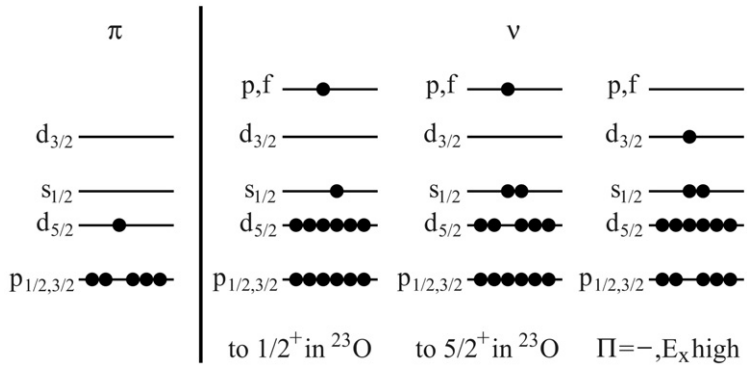

Fig. 10. Admixtures of proton and neutron excitations. The left side shows the knockout of the core (p-shell) proton. The neutron level diagrams on the right show three possible scenarios for cross shell excitations; see text for explanations (adapted from [32]).

Finally, both protons could be knocked out from the p-shell and would result in the ^{24}O configuration of $\pi(0p_{1/2,3/2})^{-2}\pi(0d_{5/2})^2$. In this case very highly excited states in ^{24}O above the one-proton separation energy are populated, which could decay to nitrogen isotopes but would more likely result in neutrons emitted sequentially from an unbound continuum of states in ^{24}O, ^{23}O and even ^{22}O. These excitations and the subsequent emission of neutrons could explain the non-resonant shape of the decay energy spectrum for ^{22}O. This is consistent with the observation of only a non-resonant background in the spectrum of the decay of ^{22}O shown in the bottom panel of Fig. 8.

The resonance at a decay energy of 45(2) keV in ^{23}O translates into an excitation energy of 2.79(13) MeV, given that the neutron separation energy is 2.74(13) MeV [33]. This assignment is based on the assumption that the neutron decays to the ground state of ^{22}O. The decay to excited states of ^{22}O is unlikely as was discussed in Ref. [13]. Recently, the observation of a $3/2^+$ state has been reported in the reaction ^{22}O(d, p) [10]. This reaction predominantly populates particle states while the present knockout reaction populates hole states. The fact that the present measurement does not populate the $3/2^+$ lends further support to the selectivity of the proposed direct reaction mechanism. The observations of the two experiments are complementary and the interpretation within the shell model has been presented in Ref. [13].

In addition to the two proton knockout $(\pi(0p_{1/2,3/2})^1, (0d_{5/2})^1)$, with subsequent emission of a neutron, the $1/2^+$ ground state and the $5/2^+$ first excited state of ^{23}O can also be populated directly by the three nucleon knockout of two protons and one neutron. The removal of two $\pi(0d_{5/2})$ protons together with a $\nu(1s_{1/2})$ or $\nu(0d_{5/2})$ neutron also populates the $1/2^+$ ground state and the $5/2^+$ state first excited state of ^{23}O, respectively. These two different mechanisms cannot be distinguished in the present experiment although this is of no consequence as they populate the same final states in ^{23}O.

Fig. 11 summarizes the population of the three oxygen isotopes within the two-proton knockout reaction mechanism. The removal of the two $d_{5/2}$ protons predominantly leads to the ground state of ^{24}O, while the removal of one $d_{5/2}$ and one p-shell proton leads to a continuum of highly excited states in ^{24}O. These proton excitations can then mix with neutron excitations as shown in Fig. 10 to populate discrete states in ^{23}O. The $5/2^+$ state is neutron unbound and decays to the ground state of ^{23}O as indicated by the arrow in Fig. 11. ^{21}O can be populated by the sequential emission of neutrons via continuum states in ^{23}O and ^{22}O.

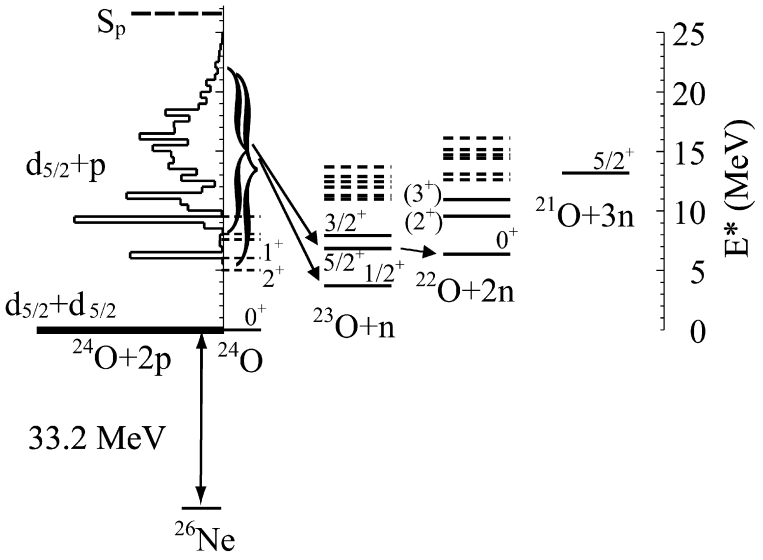

Fig. 11. Calculated proton $(d_{5/2})^1 \times (p_{1/2,3/2})^{-1}$ cross-shell excitation strength function for two-proton removal from ^{26}Ne [30,31] and the three lowest states in $^{22-24}$O (dashed lines: calculations, solid lines: experiments, adapted from [34]).

5. Conclusions

We have studied the two-proton removal reaction from ^{26}Ne populating several neutron-rich oxygen isotopes. The data were interpreted with a reaction model that includes the knock out of valence and core protons. The knock out of the valence protons is consistent with the non-observation (or at most weak population) of excited states in ^{24}O. The knock-out of one valence and one core proton leads to the selective population of the $5/2^+$ excited state in ^{23}O which we observed at a resonance energy of 45(2) keV, corresponding to a neutron-unbound resonance in ^{23}O at 2.79(13) MeV.

Acknowledgements

We would like to thank the members of the MoNA Collaboration G. Christian, C. Hoffman, K.L. Jones, K.W. Kemper, P.V. Pancella, G.F. Peaslee, W.F. Rogers, S.L. Tabor, and approximately 50 undergraduate students for their contributions to this work. We would like to thank R.A. Kryger, C. Simenel, J.R. Terry, and K. Yoneda for their valuable help during the experiment. Financial support from the National Science Foundation under grant Nos. PHY-0110253, PHY-0354920, PHY-0555366, PHY-0555445, and PHY-0606007 is gratefully acknowledged. J.E.F. and J.T. acknowledge support from the Research Excellence Fund of Michigan and from the United Kingdom Science Technology Facilities Council (STFC) under Grant No. EP/D003628, respectively.

References

[1] A. Navin, et al., Phys. Rev. Lett. 85 (2000) 266.
[2] Zs. Dombradi, et al., Phys. Rev. Lett. 96 (2006) 182501.

[3] B.A. Brown, Prog. Part. Nucl. Phys. 47 (2001) 517.
[4] B.A. Brown, in: E. Gadioli (Ed.), Proceedings of the 10th International Conference on Nuclear Reaction Mechanisms, Ricerca Scientifica ed Educazione Permanente, Supplemento N. 122, Varenna, Italy, 9–13 June 2003, p. 41.
[5] T. Otsuka, R. Fujimoto, Y. Utsuno, B.A. Brown, M. Honma, T. Mizusaki, Phys. Rev. Lett. 87 (2001) 082502.
[6] T. Otsuka, T. Suzuki, R. Fujimoto, H. Grawe, Y. Akaishi, Phys. Rev. Lett. 95 (2005) 232502.
[7] T. Otsuka, T. Matsuo, D. Abe, Phys. Rev. Lett. 97 (2006) 162501.
[8] A. Ozawa, T. Kobayashi, T. Suzuki, K. Yoshida, I. Tanihata, Phys. Rev. Lett. 84 (2000) 5493.
[9] M. Staniou, et al., Phys. Rev. C 69 (2004) 034312.
[10] Z. Elekes, et al., Phys. Rev. Lett. 98 (2007) 102502.
[11] C.R. Hoffman, et al., Phys. Rev. Lett. 100 (2008) 152502.
[12] P.G. Thirolf, et al., Phys. Lett. B 485 (2000) 16.
[13] A. Schiller, et al., Phys. Rev. Lett. 99 (2007) 112501.
[14] D. Bazin, et al., Phys. Rev. Lett. 91 (2003) 012501.
[15] D. Warner, Nature 425 (2003) 570.
[16] D.J. Morrissey, et al., Nucl. Instrum. Methods B 204 (2003) 90.
[17] Á. Horváth, et al., Eur. Phys. J. A 27 (Suppl. 1) (2006) 217.
[18] A. Schiller, et al., AIP Conf. Proc. 831 (2006) 92.
[19] M.D. Bird, et al., IEEE Trans. Appl. Superconductivity 15 (2005) 1252.
[20] B. Luther, et al., Nucl. Instrum. Methods A 505 (2003) 33.
[21] T. Baumann, et al., Nucl. Instrum. Methods A 543 (2005) 517.
[22] N. Frank, A. Schiller, D. Bazin, W.A. Peters, M. Thoennessen, Nucl. Instrum. Methods A 580 (2007) 1478.
[23] K. Makino, M. Berz, Nucl. Instrum. Methods A 558 (2005) 346.
[24] N. Frank, et al., in: Proceedings of the International Conference on Proton Emitting Nuclei and Related Topics, AIP Conf. Proc. 961 (2007) 143.
[25] R.J. Glauber, in: W.E. Brittin (Ed.), Lectures in Theoretical Physics, vol. 1, Interscience, New York, 1959, p. 315.
[26] A.M. Lane, R.G. Thomas, Rev. Mod. Phys. 30 (1958) 257.
[27] F. Deák, A. Kiss, Z. Seres, G. Caskey, A. Galonsky, B. Remington, Nucl. Instrum. Methods A 258 (1987) 67.
[28] J.R. Terry, et al., Phys. Lett. B 640 (2006) 86.
[29] J.A. Tostevin, B.A. Brown, Phys. Rev. C 74 (2006) 064604.
[30] B.A. Brown, W.A. Richter, Phys. Rev. C 72 (2005) 057301.
[31] B.A. Brown, W.A. Richter, Phys. Rev. C 74 (2006) 034315.
[32] N. Frank, et al., in: W. Bauer, R. Bellwied, J.W. Harris (Eds.), Proceedings of the 23rd Winter Workshop on Nuclear Dynamics, EP Systema, Budapest, Hungary, 2007, p. 187.
[33] G. Audi, A.H. Wapstra, C. Thibault, J. Blachot, O. Bersillon, Nucl. Phys. A 729 (2003) 337.
[34] N. Frank, et al., in: A. Covello (Ed.), Proceedings of the 9th International Spring Seminar on Nuclear Physics, World Scientific, 2008, p. 23.